# Photoemission and quantum chemical study of $SrTiO_3(001)$ surfaces and their interaction with $CO_2$

J. D. Baniecki,* M. Ishii, K. Kurihara, and K. Yamanaka
*Fujitsu Limited, 10-1 Morinosato-Wakamiya, Atsugi 243-0197, Japan*

T. Yano
*Department of Chemistry and Materials Science, Tokyo Institute of Technology, Ookayama, Meguro-ku, Tokyo 152-8550, Japan*

K. Shinozaki
*Department of Metallurgy and Ceramic Science, Tokyo Institute of Technology, Ookayama, Meguro-ku, Tokyo 152-8550, Japan*

T. Imada, K. Nozaki, and N. Kin
*Fujitsu Laboratories Ltd., 10-1 Morinosato-Wakamiya, Atsugi 243-0197, Japan*
(Received 2 November 2007; revised manuscript received 12 June 2008; published 14 November 2008)

The electronic structure of $SrTiO_3$ single-crystal surfaces and their interaction with $CO_2$ at room temperature is studied by angle-resolved x-ray and ultraviolet photoelectron spectroscopies (XPS and UPS) and density-functional theory (DFT). $CO_2$ exposure results in spectral features in the O 1*s* and C 1*s* core levels with a binding-energy separation $\Delta E_{(O\ 1s-C\ 1s)}=242.1\pm0.2$ eV. No measurable influence of $CO_2$ exposure on Sr and Ti core level spectra is observed. Adsorbate induced changes in XPS core levels and UPS valence-band spectra do not support $SrCO_3$ formation. Surface sites and bonding geometry of chemisorbed $CO_2$ on $SrTiO_3(001)$ surfaces are investigated using DFT-adsorbate-slab calculations and the calculated surface density of states compared to UPS spectra. On defect free surfaces and at lower coverages ($\Theta<0.2$), $CO_2$ is predicted to strongly bond ($E_{ads}\sim-1$ eV) to both SrO and $TiO_2$ terminated surfaces in a monodentate structure with the C atom above a lattice oxygen. Adsorption energies, electron transfer to adsorbate, and bonding geometry are found to be strongly coverage dependent with smaller adsorption energies on $TiO_2$ terminated surfaces at higher coverages. These results have important implications for the identification of metal-carbonate layers on perovskite-structure metal titanate materials by photoemission spectroscopies.

DOI: 10.1103/PhysRevB.78.195415 PACS number(s): 68.43.−h, 79.60.Dp, 73.20.Hb, 81.65.−b

## I. INTRODUCTION

Achieving a fundamental understanding of the electronic structure of perovskite-structure metal titanate ($ATiO_3$) surfaces, and their interaction with adsorbates and metal over layers, is of great scientific interest owing to the immense technological importance of this class of materials for use as dielectrics in voltage tunable capacitor and decoupling applications, as ferroelectrics in nonvolatile memory applications, as substrates or film components of high-$T_c$ superconductor-based heterostructures, as resistive switching memory elements, and as materials for catalysis, gas sensing, and gas separation.[1] Of particular significance is the identification of features in core-level photoemission spectra that are characteristic of the pristine surface, as well as their origin, and the effect of adsorbates on the surface electronic structure.[2] Such interesting fundamental questions are also of paramount practical importance when photoelectron spectroscopies are used as a surface characterization tool to deduce the presence of adsorbates or secondary phase material layers on the surface or in the near surface region of $ATiO_3$ materials. $CO_2$ chemisorption has proved to be of particular concern over the years in perovskite-structure oxide materials owing to the strong corrosion of $YBa_2Cu_3O_{7-x}$, and related high-$T_c$ oxide superconductors,[3] when exposed to $CO_2$ resulting in a decomposed surface layer consisting of $BaCO_3$, CuO, and $Y_2BaCuO_5$.[4] More recently, the potential corrosion of perovskite-structure oxide surfaces exposed to $CO_2$ has gained renewed and wide-ranging interest owing to the advancement of applications of thin films of $ATiO_3$ materials and to the sensitivity of the dielectric properties of $ATiO_3$ thin films to the surface structure.[5,6]

The literature presents a contradictory and unclear picture of the electronic structure of $ATiO_3$ surfaces and their interaction with $CO_2$ as deduced from core-level photoemission spectra. For $BaTiO_3$, the simultaneous presence of a surface related Ba core-level spin-orbit-split (SOS) pair shifted approximately 1.5 eV to higher binding energies (HBEs) from the corresponding bulk perovskite 12-fold oxygen coordinated Ba photoemission line (resulting in BEs for the surface related Ba core-level feature close to that characteristic of Ba in $BaCO_3$), with peaks in the C 1*s* and O 1*s* photoemission spectra in the range, when referenced to the hydrocarbon line at 284.6 eV, of 288–289 eV and near 531 eV, respectively, is often regarded as a definitive signature of $BaCO_3$.[7] Similar observations have been made for the Sr 3*d* core-level photoemission line of micromechanically polished[8] and annealed[9] bulk single-crystal $SrTiO_3$, as well as $(Ba,Sr)TiO_3$ (Ref. 6) and $SrTiO_3$ thin films,[10] where a surface related Sr 3*d* core level, shifted approximately 1 eV to higher BEs from the corresponding bulk 12-fold oxygen coordinated Sr 3*d* photoemission line, has been observed. Depending on the sample history or surface treatment, interpretations of the Sr 3*d* surface core-level shift (SCLS) include Sr-COH surface

 

species,[8] $SrO_x$ layers,[9] or $SrCO_3$ formed by reaction of the perovskite surface with $CO_2$ in the air.[10] However, comparable surface core-level shifts of the Ba 5*p*, 4*d*, 3*d*, and Sr 3*d* core levels are also observed for pristine vacuum-fractured surfaces of single-crystal $BaTiO_3(001)$ (Ref. 11) and $SrTiO_3(001)$ (Ref. 12) and explained by near surface Ba or Sr which is undercoordinated by oxygen resulting in a decrease in the negative Madelung potential and a corresponding shift of the surface core-level photoemission lines to higher BEs. A higher binding-energy K 2*p* doublet has also been observed for freshly scraped and $CO_2$ exposed scraped $KNbO_3$ surfaces and attributed to $K_2CO_3$ formation.[13] To understand the surface chemistry of $CO_2$ adsorption on $ATiO_3$ surfaces it is necessary to understand if surface core-level features in the photoemission spectra are correlated. As interaction among different adsorbates commonly present on air exposed $ATiO_3$ surfaces may alter photoemission core-level spectra, a preferred method to investigate adsorbate-surface interaction is to first characterize the electronic structure of the clean surface and then to introduce gas or vapor phase molecules *in vacuo*. Here we investigate the electronic structure of pristine vacuum-fractured $SrTiO_3(001)$ single-crystal surfaces and their interaction with $CO_2$ using angle-resolved x-ray and ultraviolet photoelectron spectroscopies (ARXPS and UPS). The results are compared with $CO_2$ adsorption on predominantly $TiO_2$ terminated $SrTiO_3(001)$ surfaces exhibiting atomically smooth terraces and unit-cell steps and to density-functional theory (DFT) adsorbate-slab calculations for $CO_2$ adsorption on $SrTiO_3(001)$.

## II. EXPERIMENTAL DETAILS

ARXPS measurements were performed in customized x-ray photoelectron spectroscopy (XPS) instruments by ULVAC PHI Co., Ltd. using monochromatic Al $K\alpha$ (1486.6 eV) radiation. High resolution angle-resolved photoemission spectra were recorded with a pass energy of 23.5 eV and an overall experimental resolution of less than 0.5 eV. UPS spectra were recorded at a take off angle (TOA) of 75° using He I ($h\nu$=21.2 eV) and He II ($h\nu$=40.8 eV) radiations with a pass energy of 1.2 eV. A low-energy electron flood gun was used to reduce surface charging. Reported binding energies (BEs) are not corrected for residual charge-up shift. Insulating single-crystal $SrTiO_3(001)$ samples purchased from Furuuchi Chemical Corporation were fractured parallel to the (100) planes *in vacuo* at a pressure of $1.5\times10^{-10}$ Torr yielding an irregularly stepped unreconstructed surface, with step facet normals within a few degrees of the [100] axis (Fig. 1). The surface obtained by this procedure was initially free of carbon to within the detection limits of XPS. After characterizing the pristine vacuum-fractured surface, $CO_2$ gas (99.99%) was introduced at room temperature *in vacuo* and the photoemission spectra were remeasured. Samples were dosed through a leak valve to the sample for doses up to $\sim10^3$ L (1 L=$1\times10^{-6}$ Torr s). The same adsorbate induced spectral features were observed over the exposure range with only spectral feature intensity varying. Reported doses are $\sim10^3$ L.

$TiO_2$ terminated $SrTiO_3(001)$ surfaces prepared by buffered HF etching were purchased from Shinkosha Co. Ltd.

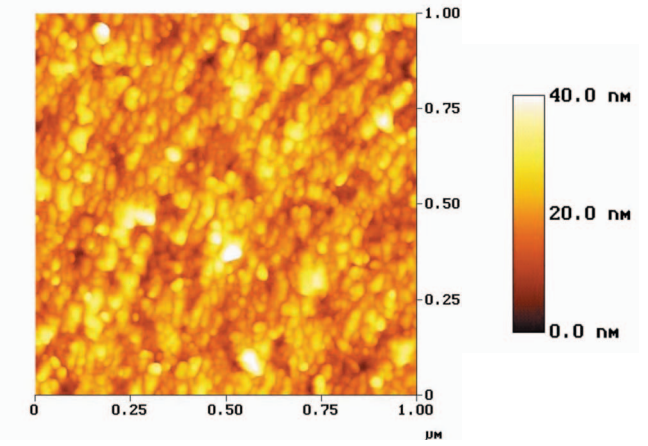


FIG. 1. (Color) Topography of $SrTiO_3(001)$ surface fractured parallel to the (100) planes *in vacuo* at a pressure of $1.5\times10^{-10}$ Torr obtained by atomic force microscopy (AFM).

The surfaces were thermal treated in a tube furnace using flowing $O_2$ at a rate of 150 *l*/*h* and heated at 650 °C for 15 min to remove hydrogen and carbon surface impurities present on the as received samples, the presence of which was confirmed by XPS and thermal-desorption spectroscopy. The resulting surface, as shown in Fig. 2, exhibited atomically smooth terraces and steps of predominantly unit-cell (3.905 Å) height. The "$TiO_2$ terminated" surface is estimated to have less than 15% SrO terminated lattice planes by XPS and atomic force microscopy (AFM). The $TiO_2$ terminated $SrTiO_3(001)$ surfaces were further thermal treated in an infrared heating chamber at 450 °C for 1 h at a pressure of $10^{-6}$ Torr and transferred *in situ* to the analysis chamber for XPS measurement. The surface obtained by this procedure exhibited a single photoemission line in the C 1*s* spectra due to hydrocarbon.

Density-functional theory calculations were performed using the periodic supercell plane-wave basis approach, as implemented in Advance/PHASE.[14] The generalized gradient approximation (GGA) as proposed by Perdew and Wang[15] was applied, combined with Vanderbilt ultrasoft pseudopotentials.[16] The plane-wave basis set was truncated at a kinetic energy of 300 eV and a $4\times4\times1$ Monkhorst-Pack[17] grid for 16 *k*-point sampling was used. Supercells were constructed of four atomic layers of alternating SrO and $TiO_2$ lattice planes and several methods of slab

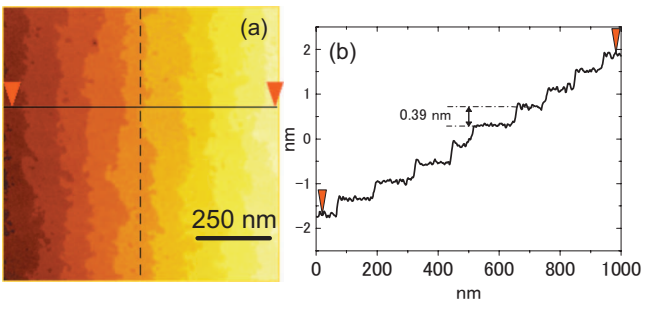


FIG. 2. (Color) Topography of a $TiO_2$ terminated surface showing a step-terrace structure with unit-cell step heights obtained by AFM.

construction were examined to investigate the effect of surface relaxation on adsorption energy and adsorbate geometry. The supercells were separated from vertical images by five layers of vacuum space.[18] These choices were guided by extensive validation tests. Structural relaxation was carried out using the conjugate gradient method with full relaxation taken to be when none of the ionic forces exceeded 0.03 eV/Å and the change in total energy was less than $2.72\times10^{-8}$ eV. Consistent with other DFT-adsorbate-slab calculations[18] spin polarized [DFT generalized gradient spin approximation (GGSA)] and unpolarized calculations resulted in a difference in adsorption energies of $\leq 0.1$ eV and almost insignificant difference in the geometry of the adsorbed molecule. As this difference is considerably less than the variation in adsorption energies due to type of surface termination and adsorbate coverage, spin polarized calculations are not presented here. Three single-point total-energy calculations were performed to determine the adsorption energy. The total energy of the gas phase adsorbent, the total energy of the surface slab without adsorbate, and the total energy of the surface slab with adsorbate are presented as follows:

$$E_{\text{ads}} = E_{(\text{slab+adsorbate})} - (E_{\text{slab}} + E_{\text{adsorbent}}).$$

Charge transfer to the $CO_2$ adsorbate and the atomic-orbital (AO) character of the energy states of the adsorbed $CO_2$ molecule was analyzed by projecting the density of states of the adsorbate-slab structure onto the $2s$ and $2p$ atomic orbitals of the oxygen and carbon atoms of the $CO_2$ molecule. A projector radius of 1.1 Å was used for both C and O. Periodic-slab DFT calculations were performed for $CO_2$ adsorption on both planar SrO and $TiO_2$ terminated $SrTiO_3(001)$ surfaces and adsorption at under coordinated sites (kinklike and steplike) was also considered. Coverages $\theta$ of 0.125 (0.08), 0.25 (0.17), and 0.5 (0.33) were obtained by studying single molecules adsorbed on SrO ($TiO_2$) surfaces with supercell lateral sizes of $1\times1$, $\sqrt{2}\times\sqrt{2}$, and $2\times2$ unit cells. Chemisorption of $CO_2$ was investigated above both anion and cation sites on SrO and $TiO_2$ terminated surfaces and for monodenate, bidenate, side-on, and end-on adsorption geometries.[19]

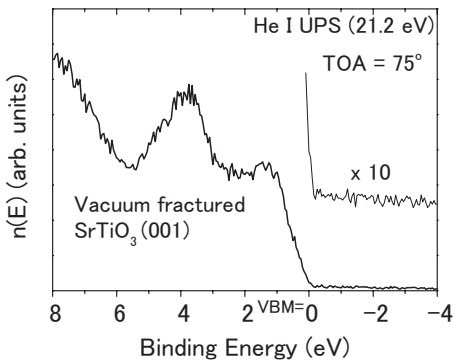


FIG. 3. He I UPS valence-band emission of the pristine vacuum-fractured surface.

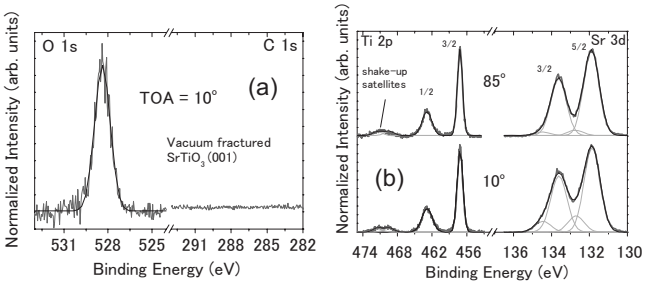


FIG. 4. (a) XPS O 1*s* and C 1*s* core-level spectra at a TOA of 10° for the pristine vacuum-fractured surface recorded just after fracture and (b) Ti 2*p* and Sr 3*d* core-level spectra of the pristine surface at take off angles of 10° and 85°. For (a) the O 1*s* and C 1*s* spectra have been normalized by their respective sensitivity factors, while for (b) at each angle the spectra are normalized to the maximum peak height for the given spectra.

## III. SURFACE ELECTRONIC STRUCTURE AND $CO_2$ EXPOSURE OF VACUUM-FRACTURED AND $TiO_2$ TERMINATED $SrTiO_3(001)$ SURFACES

He I UPS valence-band (VB) emission of the pristine vacuum-fractured surface (Fig. 3) shows a well-defined two peak structure extending approximately 6 eV below the valence-band maximum (VBM). The feature near 1 eV corresponds to the O 2*p* nonbonding states, while the peak structure near 4 eV is due to bonding between the O 2*p* and Ti 3*d* states.[20] As shown in Fig. 3, negligible emission is observed from the band-gap region.

Figure 4(a) shows the XPS O 1*s* and C 1*s* core-level spectra at a TOA of 10° for the pristine vacuum-fractured surface recorded just after fracture. The O 1*s* and C 1*s* spectra have been normalized by their respective sensitivity factors.[21] As shown in Fig. 4(a) the vacuum-fractured surface is initially free of carbon to within the detection limits of XPS and the O 1*s* spectra are representative of a single chemical state (perovskite) of oxygen. Figure 4(b) shows the Ti 2*p* and Sr 3*d* core-level spectra of the pristine surface at take off angles of 10° and 85°. At each angle the spectra are normalized to the maximum peak height for the given spectra. The line shape of the Sr 3*d* core-level spectra is angle dependent requiring two SOS pairs to describe the data if a single set of fitting parameters is used for both take off angles. Owing to the increased surface sensitivity for the spectra recorded at a TOA of 10° and the increase in relative intensity of the

TABLE I. XPS core-level separations for vacuum-fractured $SrTiO_3(001)$ and predominantly $TiO_2$ terminated $SrTiO_3(001)$ single-crystal surfaces.

| Core levels | $\Delta E$ (eV) Vacuum fractured | | $\Delta E$ (eV) $TiO_2$ term | |
|---|---|---|---|---|
| O 1*s*-Sr $3d_{5/2}$ | 396.4 | ±0.2 | 396.4 | ±0.2 |
| Sr DS-3*d* | 1.75 | ±0.1 | 1.73 | ±0.1 |
| Sr SS-3*d* | 0.90 | ±0.1 | 0.93 | ±0.1 |
| O 1*s*-Ti $2p_{3/2}$ | 71.1 | ±0.2 | 71.1 | ±0.2 |
| Ti DS-2*p* | 5.7 | ±0.1 | 5.7 | ±0.1 |

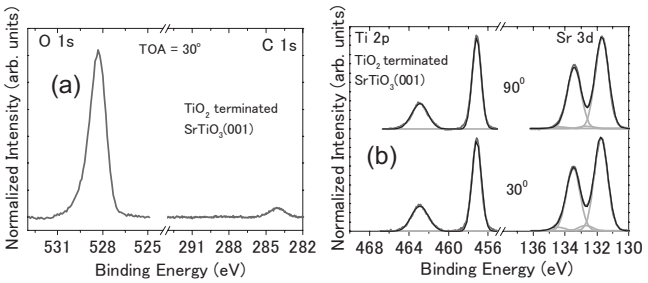


FIG. 5. (a) XPS O 1*s* and C 1*s* core-level spectra at a TOA of 30° for the $TiO_2$ terminated surface and (b) Ti 2*p* and Sr 3*d* core-level spectra of the $TiO_2$ terminated surface at take off angles of 30° and 90°. For (a) the O 1*s* and C 1*s* spectra have been normalized by their respective sensitivity factors, while for (b) at each angle the spectra are normalized to the maximum peak height for the given spectra.

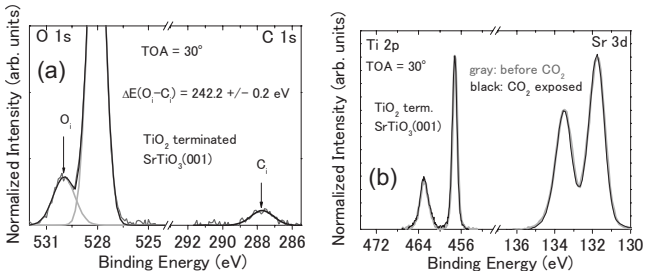


FIG. 7. (a) O 1*s* and C 1*s* photoemission spectra at a take off angle of 30° for the $CO_2$ exposed $TiO_2$ terminated surface and (b) Ti 2*p* and Sr 3*d* core-level spectra of the $TiO_2$ terminated surface before and after $CO_2$ exposure at a take off angle of 30°. For (a) the spectra have been normalized to their respective sensitivity factors, while for (b) the spectra are normalized to the maximum peak height of the respective pristine spectra.

higher binding-energy SOS pair at the lower take off angle, the higher binding-energy SOS pair originates from the near surface. Fitting the Sr 3*d* spectra to two SOS pairs of Gaussian peaks with the same widths, splitting, and relative amplitudes yields a Sr 3*d* SCLS of $+0.9 \pm 0.1$ eV which is close to the Sr 3*d* SCLS reported by Brookes *et al.*[12] (−1.0 eV) at $h\nu = 180$ eV for vacuum-fractured $SrTiO_3(001)$. In contrast to the Sr 3*d* spectra, the Ti 2*p* core-level line shape is not angle dependent and is well represented by a single SOS pair characteristic of Ti in the valence state $Ti^{+4}$. This observation is consistent with that reported for isoelectronic $BaTiO_3$ where no SCLS was observed in the XPS ($h\nu = 1486.6$ eV) Ti 2*p* core-level spectra.[20]

Core-level binding-energy separations for the vacuum-fractured surface are listed in Table I and are in good agreement with core-level binding-energy differences for $SrTiO_3(001)$ crystals as reported by Vasquez *et al.*:[22] $\Delta E_{O\ 1s-Sr\ 3d_{5/2}} = 396.5$ eV, $\Delta E_{O\ 1s-Ti\ 2p_{3/2}} = 71.1$ eV. XPS derived atomic concentration ratios indicate, within measurement accuracy, a stoichiometric near surface region: Ti/(Sr+Ti)=0.50, O/(Sr+Ti)=1.5 at 10° and 85°. The lack of band-gap emission in the He I UPS spectra and no measurable $Ti^{+3}$ emission in the Ti 2*p* XPS spectra are consistent with a low density of oxygen vacancy defects at the surface of the vacuum-fractured $SrTiO_3(001)$ crystal. These observations support the interpretation[12] that the Sr 3*d* SCLS observed in Fig. 2(b) is a feature characteristic of the pristine stoichiometric vacuum-fractured $SrTiO_3$ surface.

Figure 5 shows the O 1*s* and C 1*s* core levels [Fig. 5(a)] at a TOA of 30° and the Ti 2*p* and Sr 3*d* core levels [Fig. 5(b)] at TOAs of 30° and 90° for the $TiO_2$ terminated $SrTiO_3(001)$ surface shown in Fig. 2 exhibiting atomically smooth terraces and unit-cell steps. The energy scale has been referenced to the Ti $2p_{3/2}$ feature of the pristine vacuum-fractured surface occurring at a binding energy of 457.2 eV. The C 1*s* spectra exhibit a single photoemission line due to hydrocarbon. The Ti 2*p* core-level line shape is not angle dependent, while the Sr 3*d* line shape exhibits a small change with TOA that can be accounted for by a higher binding-energy SOS pair shifted $+0.9 \pm 0.1$ eV from the lower perovskite phase SOS pair. The similarity in SCLS with that of the fractured surface suggests that this component results from Sr ions on terminating lattice planes. From

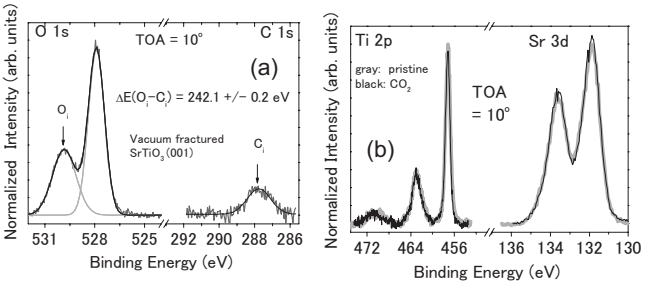


FIG. 6. (a) O 1*s* and C 1*s* photoemission spectra at a take off angle of 10° for the $CO_2$ exposed vacuum-fractured surface and (b) Ti 2*p* and Sr 3*d* core-level spectra of the pristine vacuum-fractured surface and $CO_2$ exposed surface at a take off angle of 10°. For (a) the spectra have been normalized to their respective sensitivity factors, while for (b) the spectra are normalized to the maximum peak height of the respective pristine spectra.

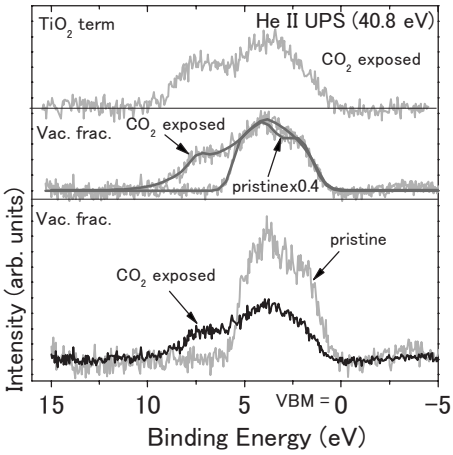


FIG. 8. He II UPS spectra of the pristine vacuum-fractured $SrTiO_3(001)$ surface and the $CO_2$ treated $SrTiO_3$ surfaces. The lower panel plots intensity versus binding energy of the pristine and $CO_2$ exposed vacuum-fractured surface for the same exposure conditions as in Fig. 6. In the middle panel the intensity of the He II UPS spectra of the pristine surface is scaled by a factor of 0.4 to compensate for attenuation of the substrate features.

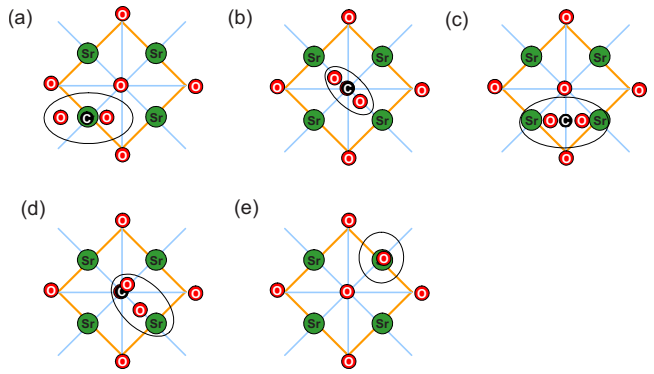


FIG. 9. (Color online) Investigated bonding configurations for $\sqrt{2}\times\sqrt{2}$ supercells of planar SrO terminated $SrTiO_3(001)$ surfaces.

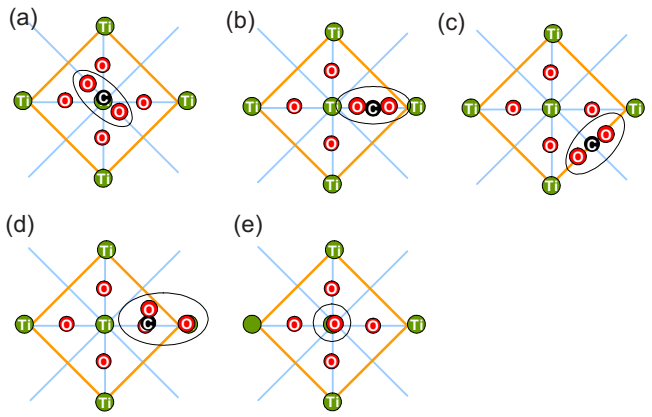


FIG. 10. (Color online) Investigated bonding configurations for $\sqrt{2}\times\sqrt{2}$ supercells of planar $TiO_2$ and terminated $SrTiO_3(001)$ surfaces.

the intensity ratio of the lower binding-energy Sr 3*d* SOS pair to the higher binding-energy SOS pair the area of $TiO_2$ terminated surface is estimated >85% which is consistent with reports of $TiO_2$ terminated surfaces prepared by similar methods to those of this study.[23]

Figure 6(a) shows the O 1*s* and C 1*s* photoemission spectra at a take off angle of 10° for the $CO_2$ exposed surface. The spectra have been normalized to their respective sensitivity factors. As seen in Fig. 6(a) $CO_2$ exposure introduces two features in the O 1*s* and C 1*s* photoemission lines. A higher binding-energy $CO_2$ exposure induced O 1*s* peak, labeled $O_i$, shifted from the perovskite phase $O_i$ peak by +1.9 eV and a single peak in the C 1*s* spectra, $C_i$, near 288 eV. The binding-energy separation between the $CO_2$ exposure induced O 1*s* and C 1*s* features is $242.1\pm0.2$ eV and the atomic concentration ratio O/C=2.7. This binding-energy difference, nearly identical to that reported for the binding-energy separation of the O 1*s* and C 1*s* photoemission peaks in $SrCO_3$ [242.1,[22] 242.0 (Ref. 24)], suggests metal-carbonate formation. However, as shown in Fig. 6(b) the Ti 2*p* and Sr 3*d* core-level spectra line shapes and intensities are nearly identical before and after $CO_2$ exposure. No measurable change in cation surface composition or correlation of the higher binding-energy Sr 3*d* SOS pair to the O 1*s* and C 1*s* $CO_2$ induced features is observed. The pristine vacuum-fractured $SrTiO_3$ surface does not decompose into a metal carbonate and Ti rich phases when exposed to $CO_2$ at room temperature. As shown in Fig. 7, similar behavior is observed for the $TiO_2$ terminated surface with nearly identical features introduced in the O 1*s* and C 1*s* photoemission lines $[\Delta E(O_i\text{-}C_i)=242.2\pm0.2$ eV] after $CO_2$ exposure.

Figure 8 shows the He II UPS spectra of the pristine vacuum-fractured $SrTiO_3(001)$ surface and the $CO_2$ treated $SrTiO_3$ surfaces. The inelastic background has been subtracted from the spectra and the energy scale referenced to the VBM. The lower panel plots intensity versus binding energy of the pristine and $CO_2$ exposed vacuum-fractured surface for the same exposure conditions as in Fig. 6. In the middle panel the intensity of the He II UPS spectra of the pristine surface is scaled by a factor of 0.4 to compensate for attenuation of the substrate features by adsorbed $CO_2$.[25] This aligns the upper edge of the O 2*p* VB for both spectra. The

TABLE II. DFT calculated carbon-lattice anion (cation) separation $d_{C\text{-}O}(d_{C\text{-}Sr})$, carbon-adsorbate oxygen bond length $d_b$, $CO_2$ oxygen-carbon-oxygen OCO angle, and adsorption energy for the specified coverages on SrO terminated $SrTiO_3(001)$ surfaces. The initial geometrical configurations of the $CO_2$ molecule are shown in Fig. 9.

| Initial configuration Figure 9 | Coverage Θ | Final configuration $d_{C\text{-}O}$ or $d_{C\text{-}Sr}$ (pm) | | $d_b$ (pm) | OCO° | Adsorption energy $E_{adsorb}$ (eV) Planar (step site) |
|---|---|---|---|---|---|---|
| (a) | 0.25 | 353.5 | ($d_{C\text{-}Sr}$) | 118.1 | 177.9 | 0.00 |
| (b) | 0.25 | 146.9 | ($d_{C\text{-}O}$) | 126.0 | 130.7 | −0.82 |
| | 0.13 | | | | | −1.25 (−1.62) |
| (c) | 0.25 | 269.2 | ($d_{C\text{-}O}$) | 118.1 | 178.3 | −0.23 |
| | 0.13 | | | | | −0.23 (−0.23) |
| (d) (side on) | 0.25 | 147.0 | ($d_{C\text{-}O}$) | 126.0 | 130.6 | −0.82 |
| (e) (end on) | 0.25 | 291.9 | ($d_{C\text{-}Sr}$) | 118.3[a]/117.6 | 180.0 | −0.10 |
| | 0.13 | | | | | −0.14 (−0.14) |

[a]C-O bond nearer surface.

TABLE III. DFT calculated carbon-lattice anion (cation) separation $d_{C\text{-}O}(d_{C\text{-}Ti})$, carbon-adsorbate oxygen bond length $d_b$, $CO_2$ oxygen-carbon-oxygen OCO angle, and adsorption energy for the specified coverage on $TiO_2$ terminated $SrTiO_3(001)$ surfaces. The initial geometrical configurations of the $CO_2$ molecule are shown in Fig. 10.

| Initial configuration Figure 10 | Coverage Θ | Final configuration $d_{C\text{-}O}$ or $d_{C\text{-}Ti}$ (pm) | | $d_b$ (pm) | OCO° | Adsorption energy $E_{adsorb}$ (eV) Planar (step site) |
|---|---|---|---|---|---|---|
| (a) | 0.17 | 353.5 | ($d_{C\text{-}Ti}$) | 118.1 | 177.9 | 0.00 |
| (b) | 0.17 | 139.1 | ($d_{C\text{-}O}$) | 127.0 | 132.3 | −0.97 |
| | 0.08 | | | | | −0.97 (−1.37) |
| (c) | 0.17 | 295.0 | ($d_{C\text{-}O}$) | 118.1 | 177.4 | −0.08 |
| | 0.08 | | | | | −0.09 (−0.23) |
| (d) (side on) | 0.17 | 139.1 | ($d_{C\text{-}O}$) | 127.0 | 132.3 | −0.97 |
| (e) (end on) | 0.17 | 271.1 | ($d_{C\text{-}Ti}$) | 117.6[a]/118.3 | 180.0 | −0.09 |
| | 0.08 | | | | | −0.10 (−0.10) |

[a]C-O bond nearer surface.

upper panel shows the UPS spectra of the $CO_2$ exposed $TiO_2$ terminated surface. The $CO_2$ exposed surfaces exhibit markedly enhanced photoemission for binding energies in the range of 5–9 eV below the VBM and some change in line shape of the O $2p$ VB in the region of 2–4 eV below the VBM may also be discerned (middle panel). No $CO_2$ induced emission is observed above 10 eV. The He II UPS spectrum of Fig. 8 is different from reported VB photoemission spectra of oxide surfaces exposed to $CO_2$ where metal-carbonate formation is thought to occur owing to the lack of emission in the range of 11–13 eV due to photoemission from the $4a_1'$ molecular orbital (MO) of $CO_3^{2-}$.[26] The lack of emission for binding energies greater than 10 eV above the VBM is also different from that reported VB features of physisorbed $CO_2$ on oxide surfaces which often exhibit photoemission from at least one molecular orbital ($1\pi_u/3\sigma_u$ and/or $4\sigma_g$), taking into account relaxation-polarization BE shift, in the binding-energy range above 10 eV (Ref. 27) (see also Figs. 15 and 18).

## IV. DENSITY-FUNCTIONAL THEORY ADSORBATE-SLAB CALCULATIONS

In addition to metal-carbonate formation, $CO_2$-$ATiO_3$ surface interaction may occur through dipole-dipole or electron transfer mediated interactions resulting in no change in the $SrTiO_3$ surface stoichiometry. Infrared spectroscopy studies of bulk $BaTiO_3$ have suggested surface carbonatelike species on $CO_2$ exposed $BaTiO_3$ surfaces with adsorbate-substrate interaction strongly influence by the ferroelectric surface bound charge.[28] This viewpoint[29,30] has been emphasized for polycrystalline $BaTiO_3$ ceramics where the absence of detectable carbonate species was regarded as evidence for suppression of spontaneous polarization in fine grained ferroelectric materials.[31] While ionic adsorbates do interact with ferroelectric surface bound charge, stabilizing the monodomain ferroelectric phase in $PbTiO_3$ thin films,[2] bulk single-crystal $SrTiO_3(001)$ is predicted to exhibit only a weak surface ferroelectric instability easily destroyed by thermal fluctuations at room temperature.[32]

### A. $CO_2$ adsorption on planar $SrTiO_3(001)$ surfaces

DFT-adsorbate-slab calculations were performed to investigate $CO_2$ chemisorption on $SrTiO_3(001)$ surfaces. As shown in Figs. 9 and 10 for $\sqrt{2}\times\sqrt{2}$ supercells of planar SrO and $TiO_2$ terminated surfaces, respectively, chemisorption of $CO_2$ was investigated above both anion and cation sites and for monodenate, bidenate, side-on, and end-on adsorption geometries.[19] Initial positions obtained by rotating the molecule ±45° from that shown in Figs. 9 and 10 were also investigated. These initial configurations were not energetically favorable transforming to the final configurations given in Tables II and III. Tables II and III show the final geometric configuration and adsorption energy after total-energy minimization for the adsorption configurations shown in Figs. 9 and 10, respectively. Method III that will be discussed below was used for the calculation. For both surfaces, the lowest total energy occurs for $CO_2$ adsorption above a surface lattice oxygen in a monodentate structure with the carbon atom bonding to the surface anion. The side-on geometry shown in Figs. 9(d) and 10(d) was not stable and transformed to the same final configuration (monodentate) as that of Figs. 9(b)

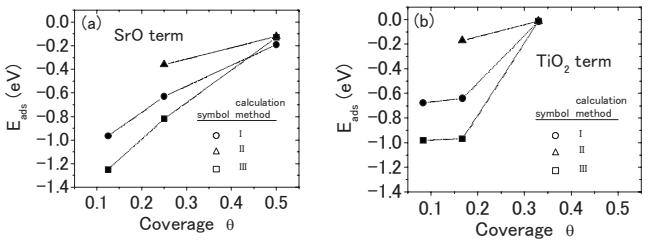


FIG. 11. Adsorption energy $E_{ads}$ as a function of coverage for (a) SrO and (b) $TiO_2$ terminated surfaces.

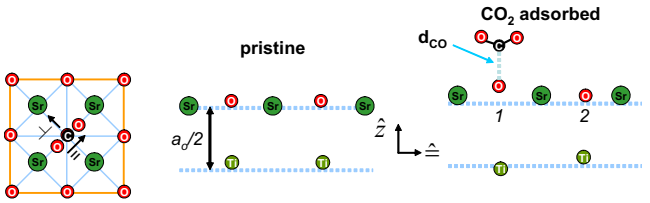


FIG. 12. (Color online) Adsorbate structure and equilibrium atomic displacements (relative to theoretical atomic positions in bulk $SrTiO_3$ $a_0$=3.90 Å) on a SrO terminated surface (2×2 supercell) for atoms in a plane containing the $z$ axis and the diagonal along the OCO axis of the $CO_2$ molecule. For the adsorbate free surface: $\delta z_{Sr}$=0.013, $\delta z_O$=0.137, and $\delta z_{Ti}$=0.146. For the adsorbate covered surface: $\delta z_{Sr}$=0.160, $\delta z_{O1}$=0.311, $\delta z_{Ti1}$=−0.063, $\delta z_{O2}$=0.136, and $\delta z_{Ti2}$=0.159. Units are in Å and positive displacement is toward vacuum region. Method (III) in Fig. 11 was used for the calculation.

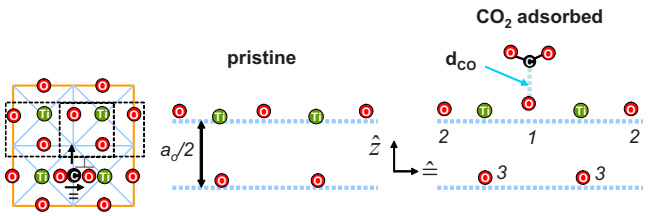


FIG. 13. (Color online) Adsorbate structure and equilibrium atomic displacements (relative to theoretical atomic positions in bulk $SrTiO_3$ $a_0$=3.9 Å) on a $TiO_2$ terminated surface (2×2 supercell) for atoms in a plane containing the $z$ axis and the diagonal along the OCO axis of the $CO_2$ molecule. For the adsorbate free surface: $\delta z_{Ti}$=0.036, $\delta z_O$=0.167 (top layer), and $\delta z_O$=0.111 (second layer). For the adsorbate covered surface: $\delta z_{Ti}$=0.143, $\delta z_{O1}$=0.200, $\delta z_{O2}$=0.294, and $\delta z_{O3}$=0.152. Units are in Å and positive displacement is toward vacuum region. Method (III) in Fig. 11 was used for the calculation.

and 10(b). For the $TiO_2$ terminated surface all other geometries are metastable at $T$=0 K. For the SrO terminated surface, a weakly bound ($E_{ads}$=−0.23 eV) structure bridging two Sr ions was found as shown in Fig. 9(c). As shown in Tables II and III the adsorption energy for configurations (a), (c), and (e) of Figs. 9 and 10 did not significantly vary with coverage.

Figure 11 shows the adsorption energy $E_{ads}$ as a function of coverage for SrO [Fig. 11(a)] and $TiO_2$ [Fig. 11(b)] terminated planar surfaces, respectively, where $CO_2$ is adsorbed above a surface lattice oxygen [corresponding to the configurations shown Figs. 9(b) and 10(b)]. Three different calculation methods are presented. The $CO_2$ molecule was geometry optimized using (I) a four layer frozen slab cleaved from geometry optimized bulk $SrTiO_3$ (calculated equilibrium lattice parameter $a_0$=3.90 Å), (II) a four layer frozen slab constructed by geometry optimization of the upper two atomic layers of a slab constructed by method (I), and (III) additional relaxation of the upper two atomic layers of a slab constructed by method (II) concurrent with geometry optimization of the $CO_2$ molecule. Method (II), used to calculate the adsorption energy of $CO_2$ on BaO surfaces,[18] predicts a significantly less stable chemisorbate than method (I) or (III) for $CO_2$ adsorption on $SrTiO_3$(001). At lower coverages where the adsorption energy is dominated by substrate-adsorbate interaction a marked influence of the magnitude of $E_{ads}$ on slab construction method is observed. At higher coverage $E_{ads}$ decreases with increasing coverage owing to lateral interactions among adsorbates. For the $TiO_2$ surface at a coverage $\Theta$=0.33 $E_{ads}$ is independent of the slab construction method and dominated by the adsorbate-adsorbate interaction. As will be discussed below, the difference in coverage dependence of $E_{ads}$ for the two surface terminations is due to the difference in geometrical arrangement of surface atoms and the different abilities of each type of surface to donate electronic charge to the adsorbed molecule.

Figures 12 and 13 show the surface-adsorbate structure and equilibrium atomic displacements (relative to theoretical atomic positions in bulk $SrTiO_3$ $a_0$=3.90 Å) on SrO and $TiO_2$ terminated planar surfaces (2×2 supercell), respectively, using calculation method (III). The cross sectional figures contain atoms in a plane containing the $z$ axis and the diagonal along the OCO axis of the $CO_2$ molecule. Both SrO and $TiO_2$ terminated pristine surfaces exhibit rumpling with the oxygen ions displaced outward toward the vacuum by $S_1$(Sr)=0.124 Å and $S_1$(Ti)=0.132 Å, respectively, and a contraction of the interlayer distance between the first two layers: $\Delta d_{12}^{SrO}/d_0$=−6.82% and $\Delta d_{12}^{TiO_2}/d_0$=−8.85%, where $d_0=a_0/2$ is the bulk interlayer spacing.[33] These atomic displacements are consistent in sign and approximate magnitude

TABLE IV. DFT calculated carbon-lattice oxygen separation $d_{CO}$, carbon-adsorbate oxygen bond length $d_b$, $CO_2$ oxygen-carbon-oxygen OCO angle, and net electron transfer to $CO_2$ for varying coverage on SrO and $TiO_2$ terminated $SrTiO_3$(001) surfaces. Method (III) in Fig. 11 was used for the calculation.

| Adsorbate-surface structure | Θ | $d_{CO}$ (pm) | $d_b$ (pm) | OCO angle (deg) | Electron transfer to $CO_2$ ($e$) |
|---|---|---|---|---|---|
| $CO_2$ (free) | | | 118.0 | 180.0 | |
| SrO 1×1 | 0.50 | 171.6 | 122.2 | 142.4 | −0.43 |
| SrO ($\sqrt{2}\times\sqrt{2}$) | 0.25 | 146.9 | 126.0 | 130.7 | −0.62 |
| SrO (2×2) | 0.125 | 141.7 | 127.4 | 129.0 | −0.68 |
| $TiO_2$ (1×1) | 0.33 | 320.1 | 117.9 | 178.5 | −0.04 |
| $TiO_2$ ($\sqrt{2}\times\sqrt{2}$) | 0.17 | 139.1 | 127.0 | 132.3 | −0.50 |
| $TiO_2$ (2×2) | 0.08 | 138.9 | 127.0 | 132.1 | −0.52 |

with recent full-potential linearized augmented plane-wave method plus local-orbital calculations[34] and low-energy electron diffraction (LEED) observations.[35] On coordination of the $CO_2$ molecule with the surface, the surface relaxation markedly changes. The bonding lattice oxygen for both surface types is displaced outward toward the $CO_2$ molecule with the bonding lattice oxygen-cation separation ($S_1$) increasing to 0.15 Å for both SrO and $TiO_2$ terminated surfaces. On the SrO surface the Ti atom below the bonding lattice oxygen is displaced away from the surface.

On planar, vacancy free surfaces, the most energetically favored geometry for chemisorption, except for the $TiO_2$ terminated surface at $\Theta=0.33$, is a monodentate configuration with the carbon atom down above a lattice oxygen and adsorbate oxygen atoms aligned to diametrically opposite nearest-neighbor surface cations. For the $TiO_2$ terminated surface at $\Theta=0.33$, this configuration results in a separation of only 1.5 Å, as compared to 2.9 Å for the SrO terminated surface, between nearest-neighbor adsorbate oxygen atoms of adjacent $1\times1$ supercells. A lower-energy configuration is obtained by rotating the molecule by 45° which aligns adsorbate oxygen atoms to diametrically opposite surface anions and increases the separation between nearest-neighbor adsorbate oxygen atoms of adjacent cells to ~3.0 Å. This geometry, as shown in Table IV, is a physisorbed type of specie metastable at $T=0$ K.

Slabs constructed using methods (I) and (III) exhibit different surface atomic configurations with (III) having a static dipole moment in the surface layer owing to rumpling and relaxation. However, both slabs predict at lower coverages $CO_2$ strongly bonds to the defect free planar $SrTiO_3$ surface with adsorption energies of −0.97 and −1.25 eV for the SrO terminated surface using calculation methods (I) and (III), respectively. For both methods, the adsorption energy is ~ −0.3 eV lower for $CO_2$ adsorption on the SrO terminated surface and can be understood in terms of the difference in basicity between the two types of surfaces. The Madelung potential, which stabilizes the anion at the surface, is less negative for oxygen sites on the SrO terminated surface (−16.85 eV) than on the $TiO_2$ terminated surface (−23.83 eV),[36] resulting in a more diffuse charge distribution around the oxygen and a lower cost for charge transfer from the surface anion to the $CO_2$ molecule.[37] This is consistent with the larger charge transfer to the $CO_2$ molecule calculated for adsorption above an anion on the SrO terminated surface (Table IV) and with cluster model calculations for $CO_2$ adsorption on MgO and CaO oxide surfaces where the larger reactivity of $CO_2$ adsorption on CaO was shown to be due to the higher basicity of CaO.[37] Geometric, energetic, and charge-transfer values for the different surface-adsorbate structures are shown in Table IV. At low coverages the chemisorbed species is very stable and resembles a carbonatelike structure (Figs. 12 and 13). For the $2\times2$ supercell structure on the SrO terminated surface, corresponding to a coverage of 0.13, $E_{ads}=-1.3$ eV, $d_{CO}=141.7$ pm, $d_b=127.4$ pm, and OCO=129.0° (for carbonate: $d_b=130$ pm and OCO=120°).[18]

### B. Adsorption at irregular surface sites

Chemisorption of $CO_2$ was investigated for the same initial configurations as shown in Figs. 9 and 10 at irregular surface sites formed, as shown in Fig. 13, by removing one (kinklike) or two (steplike) stoichiometric SrO or $TiO_2$ units from the $2\times2$ supercell surface. As shown in Tables II and III, a decrease in $E_{ads}$ is predicted for chemisorption of $CO_2$ above a lattice oxygen at steplike sites on $2\times2$ supercells. For the $TiO_2$ terminated surface, $E_{ads}$ decreases from −0.97 eV for planar surface to −1.37 eV at a step site, thus predicting increased bonding at under coordinated sites. The other bonding configurations exhibited no significant decrease in adsorption energy. On insulating $SrTiO_3(001)$ surfaces $CO_2$ is predicted to preferentially bond to a lattice oxy-

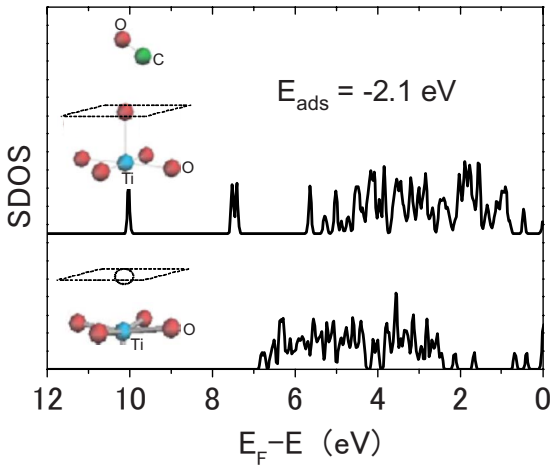


FIG. 14. (Color online) Surface density of states (SDOS) calculated for a $CO_2$ oxygen atom filling a lattice oxygen vacancy site. The surface changes from metallic to insulating after adsorption with one $CO_2$ oxygen atom filling the vacancy site and the remaining atoms forming a CO molecule.

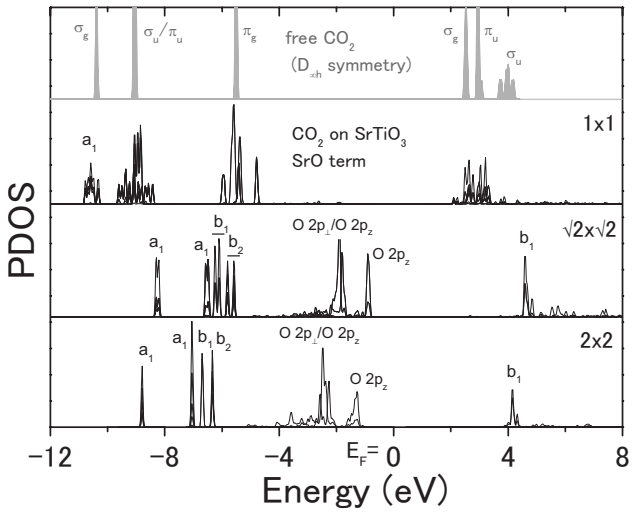


FIG. 15. Density of states projected (PDOS) onto the 2*s* and 2*p* AOs of the carbon and oxygen atoms in $CO_2$ for single molecules adsorbed above a lattice oxygen of $1\times1$, $\sqrt{2}\times\sqrt{2}$, and $2\times2$ supercells for SrO terminated surfaces. Also shown is the PDOS of free $CO_2$ in linear $D_{\infty h}$ symmetry calculated by DFT. The labeling of energy states corresponds to the symmetry specie of the projectors which yield a non-negligible PDOS for the given energy state. Method (III) in Fig. 11 was used for the calculation.

TABLE V. Projected density of states (in percent) and symmetry specie of the projectors of uncoordinated linear $CO_2$. The $2s$ and $2p$ AOs of the carbon and two oxygen atoms in $CO_2$ were used as projectors.

| Energy state | Carbon AOs | | Oxygen AOs | | |
|---|---|---|---|---|---|
| (eV) | $2s$ | $2p_{=}$, $2p_{\perp}$,$2p_z$ | $2s$ | $2p_{=}$, $2p_{\perp}$, $2p_z$ | Symmetry |
| 8.447 | 0.0 | 0.0, 26.7, 26.7 | 0.0 | 0.0, 23.3, 23.3 | $\pi_u$ |
| 8.020 | 15.0 | 0.0, 0.0, 0.0 | 41.8 | 43.2, 0.0, 0.0 | $\sigma_g$ |
| −0.014 | 0.0 | 0.0, 0.0, 0.0 | 0.0 | 0.0, 50.0, 50.0 | $\pi_g$ |
| −3.531 | 0.0 | 0.0, 18.9, 18.9 | 0.0 | 0.0, 31.1, 31.1 | $\pi_u$ |
| −3.564 | 0.0 | 19.2, 0.0, 0.0 | 12.5 | 68.3, 0.0, 0.0 | $\sigma_u$ |
| −4.887 | 21.9 | 0.0, 0.0, 0.0 | 23.3 | 54.8, 0.0, 0.0 | $\sigma_g$ |

gen in a monodentate configuration at either planar or irregular surface sites with a moderate decrease in adsorption energy at irregular surface sites.

On degenerate surfaces, not characteristic of the surfaces used in this study, formed by removing an oxygen vacancy from a $\sqrt{2}\times\sqrt{2}$ supercell (structural relaxation with three atomic layers was performed), a large decrease in adsorption energy was calculated for adsorption of $CO_2$ above a vacancy site. Other adsorption sites exhibited significantly smaller decreases in $E_{ads}$. For the SrO terminated $\sqrt{2}\times\sqrt{2}$ supercell (Fig. 9) a decrease in $E_{ads}$ from −0.82 eV (insulating) to −2.1 eV (degenerate) was calculated for adsorption of $CO_2$ in a monodentate configuration with the carbon atom displaced down toward the vacancy site. In contrast, for the linear end-on configuration of Fig. 12(e) $E_{ads}$ decreased slightly from −0.10 to −0.14 eV. An adsorption energy of −2.1 eV was also calculated for a $CO_2$ oxygen atom filling a lattice oxygen vacancy site (Fig. 14). The surface changes from metallic to insulating after adsorption with one $CO_2$ oxygen filling the vacancy site and the remaining atoms forming a CO molecule (calculated bond length: 115.98 pm and experimental CO bond length: 116.0 pm). CO desorption from reduced $SrTiO_3$(001) surfaces after $CO_2$ gas exposure has been detected by thermal-desorption spectroscopy by Azad *et al.*[38] Bond cleavage has also been calculated for adsorption of $N_2O$ above an oxygen vacancy site.[39]

### C. Surface and projected density of states of $CO_2$ adsorbed on insulating $SrTiO_3$(001) surfaces

Figure 15 shows the projected density of states (PDOS) of single $CO_2$ molecules adsorbed above a lattice oxygen of $1\times1$, $\sqrt{2}\times\sqrt{2}$, and $2\times2$ supercells for SrO terminated surfaces using the $2s$ and $2p$ AOs of the carbon and oxygen atoms in $CO_2$ as projectors. Also shown in Fig. 15 is the PDOS of free $CO_2$ in linear $D_{\infty h}$ symmetry calculated by DFT. Tables V and VI give the PDOS for the specific target AOs (in percent) for free $CO_2$ ($D_{\infty h}$ symmetry) and coordinated $CO_2$ ($2\times2$ supercell) on SrO terminated $SrTiO_3$, respectively, as well as the symmetry specie of the projectors (AOs) which yield a non-negligible PDOS for each given energy state. In Fig. 15 the energy scale for the PDOS of the adsorbed $CO_2$ is referenced to the Fermi energy which lies in the $SrTiO_3$ band gap (Fig. 16). For comparison, the energy state at −4.887 eV in Table V has been aligned to the energy states centered near −10.6 eV (labeled $a_1$) in Fig. 15 of the $CO_2$ molecule adsorbed above a lattice oxygen of a $1\times1$ cell. PDOS calculations show that these energy states have similar AO character (O $2s$, O $2p_{=}$, C $2s$). As expected and shown in Table V, the PDOS of the lowest occupied energy state in uncoordinated linear $CO_2$ is of nonbonding O $2p_{\perp z}$ (Ref. 40) AO character ($\pi_g$ symmetry), while −3.517 eV below it is an energy state of O $2p_{\perp z}$, C $2p_{\perp z}$ AO character ($\pi_u$ symmetry). This energy state is responsible for the major part of bonding in linear $CO_2$.[41] At a slightly lower energy of −3.564 eV is an energy state of predominantly O $2p_{=}$ AO character with a smaller state density also projected onto the O $2s$ and O $2p_{=}$ AOs. This is consistent with photoemission vibrational spectra and electron momentum spectroscopy which show that this energy state, associated with the $3\sigma_u$ MO in linear $CO_2$, is of nonbonding type II character with the charge distributed mainly on the oxygen atoms.[41] These calculated energy states correspond to the electronic configu-

TABLE VI. Projected density of states (in percent) and symmetry specie of the projectors of $CO_2$ adsorbed on SrO terminated $SrTiO_3$ ($2\times2$ supercell) using calculation method (III). The $2s$ and $2p$ AOs of the carbon and two oxygen atoms in $CO_2$ were used as projectors.

| Energy state | Carbon AOs | | Oxygen AOs | | Corresponding |
|---|---|---|---|---|---|
| (eV) | $2s$ | $2p_{=}$, $2p_{\perp}$,$2p_z$ | $2s$ | $2p_{=}$, $2p_{\perp}$, $2p_z$ | $C_{2v}$ symmetry |
| 4.152 | 1.3 | 0.0, 52.3, 1.9 | 3.1 | 0.0, 40.4, 1.0 | $b_1$ |
| −0.7 to −5.7 | 0.2 | 2.1, 0.0, 0.6 | 0.3 | 0.0, 53.4, 43.4 | |
| −6.343 | 0.0 | 26.0, 0.0, 0.0 | 15.1 | 35.9, 0.0, 23.0 | $b_2$ |
| −6.697 | 0.0 | 0.0, 52.0, 0.0 | 0.0 | 0.0, 48.0, 0.0 | $b_1$ |
| −7.050 | 5.4 | 0.0, 0.0, 27.6 | 11.9 | 54.0, 0.0, 1.1 | $a_1$ |
| −8.792 | 40.2 | 0.0, 0.0, 7.8 | 25.7 | 16.6, 0.0, 9.7 | $a_1$ |

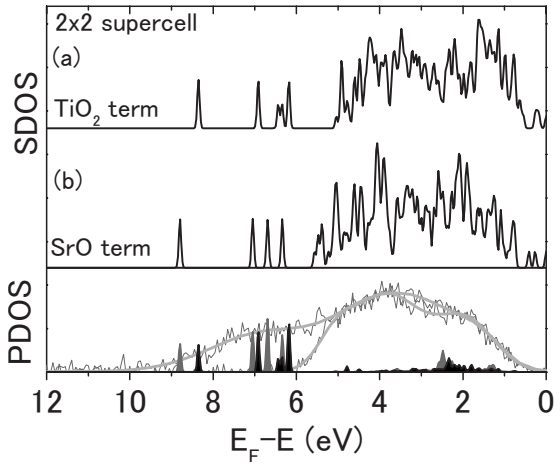


FIG. 16. Surface density of states [upper panels (a) and (b)] and PDOS [lower panel] for single $CO_2$ molecules adsorbed above a lattice oxygen of a $2\times2$ supercell for $TiO_2$ [upper panel (a)] and SrO [upper panel (b)] terminated surfaces. For comparison, the experimental UPS spectra before and after $CO_2$ exposure have also been included on the PDOS panel and aligned to the upper edge of the DFT calculated valence band. Method (III) was used for the calculation.

ration of the $X^1\Sigma_g^+$ ground state of linear $CO_2$: $4\sigma_g^2 3\sigma_u^2 1\pi_u^4 1\pi_g^4$. Orbital energy-level separations derived from photoemission vertical binding-energy positions give $1\pi_u - 1\pi_g = 3.8$ eV, $3\sigma_u - 1\pi_g = 4.3$ eV, and $4\sigma_g - 1\pi_g = 5.6$ eV.[41,42]

On coordination of the $CO_2$ molecule with the lattice oxygen the PDOS markedly changes. As shown in Fig. 15, for the $1\times1$ cell the energy separation between groups of states is comparable to that of uncoordinated linear $CO_2$. PDOS calculations show that the energy states for the $1\times1$ cell are of similar AO character as the corresponding states in the free linear $CO_2$ molecule. However, the reduction in symmetry from $D_{\infty h}$ to $C_{2v}$ causes a splitting of energy for all $\Pi$ states and for the $1\times1$ and $\sqrt{2}\times\sqrt{2}$ cells; an additional splitting of energy states owing to lateral adsorbate interaction is also discernable. This splitting disappears for isolated $CO_2$ molecules adsorbed at low coverage. For the $2\times2$ supercell four well resolved energy states occur in the range of −8.8 to −6.3 eV below the Fermi level. In the region of the valence band (−5.7 to −0.7 eV in Fig. 15) states of predominantly O $2p_{\perp z}$ AO character, with a smaller state density also projected onto the C $2p_z$, C $2p_{=}$, and O $2s$ AOs, are predicted. The next highest-energy state occurs at 4.152 eV well outside the band-gap region.

As shown in Table VI, the PDOS at energies of 4.152 and −6.697 eV is of predominantly C $2p_{\perp z}$, O $2p_{\perp}$ AO character ($b_1$ symmetry specie of the $C_{2v}$ point group). These energy states transform into the $\Pi_u$(8.447 eV) and $\Pi_u$(−3.531 eV) energy states of the free linear $CO_2$ molecule, respectively, upon dissociation of the $CO_2$ molecule from the surface. Similar to the orbital energy states associated with the $2b_1$ and $1b_1$ MOs in uncoordinated bent $CO_2^-$ in $C_{2v}$ symmetry (to which the 4.152 and −6.697 eV states, respectively, correspond), the AO character of these energy states does not significantly change as the $CO_2$ molecule bonds to the surface. The energy state at −7.050 eV, of predominantly O $2p_{=}$, C $2p_z$ AO character, also transforms to the $\Pi_u$ (−3.531 eV) energy state upon detachment of the molecule from the surface. At −6.343 eV is an energy state of C $2p_{=}$, O $2s$, O $2p_{=}$, and O $2p_z$ AO character. This energy state transforms into the $\Sigma_u$(−3.564 eV) energy state of the free linear $CO_2$ molecule after dissociation from the surface and, similar to the energy state associated with the $3b_2$ MO of free bent $CO_2^-$, takes on appreciable O $2p_z$ AO character for smaller OCO angles on bonding to the surface. The energy state at −8.792 eV transforms into the $\Sigma_g$(−4.887 eV) energy state for an uncoordinated linear $CO_2$ molecule. On coordination, this energy state also has considerable O $2p_z$ AO character, similar to the $4a_1$ MO of uncoordinated $CO_2^-$ where bending of the molecule shifts a significant fraction of charge out of the O $2p_{=}$ AO and into to the O $2p_z$ AO.[42]

The calculated PDOS of a $CO_2$ molecule adsorbed above a lattice oxygen of a SrO terminated $SrTiO_3$(001) surface (Fig. 15 and Table VI) is similar to the Hartree-Fock one-electron orbital energies of uncoordinated $CO_2^-$ in $C_{2v}$ symmetry ($4a_1^2 3b_2^2 1b_1^2 5a_1^2 4b_2^2 1a_2^2 6a_1^1$) of Freund and Messmer[43] where it was also shown that one-electron orbital contour plots of uncoordinated bent $CO_2^-$ and Ni-$CO_2^-$ complexes exhibit very similar orbital shapes. For the coordinated $CO_2^{-\delta}$ molecule the energy states corresponding to the $4b_2$, $1a_2$, and $6a_1$ orbitals of the uncoordinated $CO_2^-$ molecule lie in the valence-band region where, as shown in Table VI, states of O $2p_{\perp z}$, C $2p_{=z}$ AO character occur. This AO character is consistent with the picture[19] of $CO_2$ adsorption on oxide surfaces at oxygen anion sites described as a two electron two orbitals highest occupied molecular orbital (HOMO)–lowest unoccupied molecular orbital (LUMO) interaction involving electron transfer from the highest occupied molecular orbital of the surface oxygen ion to the empty $2\pi_u$ ($6a_1$) MO of $CO_2$ which appears at lower energy after partial filling of the orbital. Thus, while the adsorbate has a carbonatelike structure the PDOS is more similar to that of $CO_2^-$ in $C_{2v}$ symmetry than $CO_3^{-2}$ in $D_{3h}$ symmetry. The latter exhibits three energy states associated with the orbitals ($1a_2''$,$3e'$,$4a_1'$) 5–8 eV below the O $2p$ nonbonding orbitals,[44] while Fig. 15 shows four energy states of similar AO character to the orbital energy states of uncoordinated bent $CO_2^-$. For the coordinated $CO_2^{-\delta}$ molecule, the ordering of the energy states depends on both lateral adsorbate and adsorbate-substrate interaction.

Figure 16 shows the surface density of states (SDOS) of the adsorbate-slab structure of $TiO_2$ [upper panel (a)] and SrO [upper panel (b)] terminated surfaces for single $CO_2^{-\delta}$ molecules adsorbed above a lattice oxygen of a $2\times2$ supercell. The lower panel plots the PDOS (using the carbon and oxygen AOs of the adsorbed $CO_2$ as projectors) for the surfaces of upper panels (a) and (b). For comparison, the experimental UPS spectra before and after $CO_2$ exposure have also been included on the PDOS panel and aligned approximately to the upper edge of the DFT calculated valence band. In general agreement with the UPS spectra, the DFT calculated SDOS predicts energy states associated with $CO_2$ adsorption in a monodentate structure above a lattice anion on both SrO and $TiO_2$ terminated surfaces in the range of 6–9 eV below the VBM [similar SDOS is also obtained for the $\sqrt{2}\times\sqrt{2}$ cell with the adsorbate induced states appearing

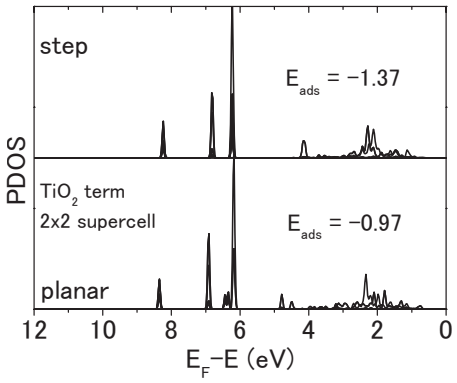


FIG. 17. PDOS for adsorption above lattice oxygen in a monodentate configuration at a planar and step site.

at slightly higher energies (−0.3 eV)]. As shown in Fig. 17, adsorption above a lattice oxygen in a monodentate configuration at step sites yielded a similar PDOS. The experimental UPS spectra are thus consistent with emission from different monodentate bonding configurations including bonding at lattice oxygen sites on planar SrO or $TiO_2$ terminated lattice planes and at irregular surface sites. In contrast, as shown in Fig. 18, the other bonding configurations did not yield SDOS consistent with the experimental data.

## V. CONCLUSION

In summary, exposure of pristine vacuum-fractured and $TiO_2$ terminated $SrTiO_3$(001) surfaces to $CO_2$ at room temperature results in spectral features in the O 1*s* and C 1*s* core levels with a binding-energy separation $\Delta E_{(\mathrm{O}\ 1s\text{-}\mathrm{C}\ 1s)} = 242.1 \pm 0.2$ eV while no measurable influence on Sr and Ti core levels was observed. Adsorbate induced changes in XPS core levels and UPS valence-band spectra do not support $SrCO_3$ formation at room temperature. DFT-adsorbate-slab calculations predict on defect free surfaces, and at lower coverages ($\Theta < 0.2$), $CO_2$ strongly bonds ($E_{\mathrm{ads}} \sim -1$ eV) to both SrO and $TiO_2$ terminated surfaces in a bent monodentate structure with the C atom above a lattice oxygen. While the adsorbate has a carbonatelike structure, the PDOS is more similar to that of $CO_2^-$ in $C_{2v}$ symmetry than $CO_3^{-2}$ in $D_{3h}$ symmetry. These results demonstrate the difficulty in identification of metal-carbonate layers on the surface or in the near surface region of $ATiO_3$ materials by x-ray photoemission spectroscopy. The difficulty arising due to the possibility of chemisorbed $CO_2$ and metal-carbonate surface layers yielding similar photoemission spectra owing to the nearly identical O 1*s*-C 1*s* core-level BE difference and to the close proximity of the perovskite A site cation HBE surface state, resulting from lower oxygen coordination on the surface (eightfold) than in the bulk (12-fold), with the BE state of the ninefold oxygen coordinated cation in $MCO_3$.[45]

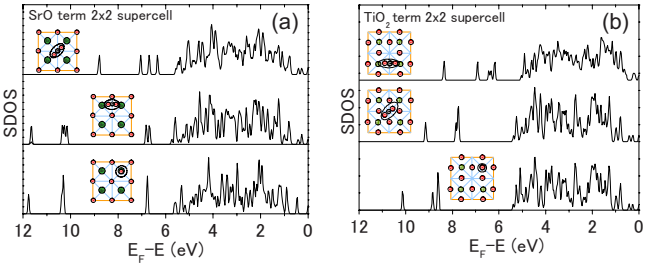


FIG. 18. (Color online) SDOS for different bonding configurations considered in the text. (a) $2\times2$ SrO terminated $SrTiO_3$(001) surface: top panel (monodentate) $E_{\mathrm{ads}}=-1.25$ eV, middle panel (Sr bridging) $E_{\mathrm{ads}}=-0.23$ eV, and lower panel (end on) $E_{\mathrm{ads}}=-0.14$ eV. (b) $2\times2$ $TiO_2$ terminated $SrTiO_3$(001) surface: top panel (monodentate) $E_{\mathrm{ads}}=-0.97$ eV, middle panel $E_{\mathrm{ads}}=-0.1$ eV, and lower panel (end on) $E_{\mathrm{ads}}=-0.1$ eV.

## ACKNOWLEDGMENTS

The authors are indebted to P. C. McIntyre and R. J. Zednik for fruitful discussions and thank R. L. Kurtz and L. T. Hudson for discussing aspects of their earlier work. This work was supported in part by the Ministry of Internal Affairs and Communication (MIC) of Japan through "Research and development of fundamental technologies for advanced radio frequency spectrum sharing in mobile communication systems."

*baniecki@labs.fujitsu.com

[1] *Nanoelectronics and Information Technology*, edited by R. Waser (Wiley, New York, 2003).
[2] D. D. Fong, A. M. Kolpak, J. A. Eastman, S. K. Streiffer, P. H. Fuoss, G. B. Stephenson, C. Thompson, D. M. Kim, K. J. Choi, C. B. Eom, I. Grinberg, and A. M. Rappe, Phys. Rev. Lett. **96**, 127601 (2006).
[3] R. L. Kurtz, R. Stockbauer, and T. E. Madey, Phys. Rev. B **37**, 7936 (1988).
[4] T. H. Buyuklimanli and J. H. Simmons, Phys. Rev. B **44**, 727 (1991).
[5] M. Kurasawa and P. C. McIntyre, J. Appl. Phys. **97**, 104110 (2005).
[6] J. D. Baniecki, M. Ishii, T. Shioga, K. Kurihara, and S. Miyahara, Appl. Phys. Lett. **89**, 162908 (2006).
[7] C. Miot, E. Husson, C. Proust, R. Erre, and J. P. Coutures, J. Mater. Res. **12**, 2388 (1997).
[8] P. A. W. van der Heide, Q. D. Jiang, Y. S. Kim, and J. W. Rabalais, Surf. Sci. **473**, 59 (2001).
[9] K. Szot, W. Speier, U. Breuer, R. Meyer, J. Szade, and R. Waser, Surf. Sci. **460**, 112 (2000).
[10] S. Bhaskar, D. Allgeyer, and J. A. Smythe III, Appl. Phys. Lett. **89**, 254103 (2006).
[11] L. T. Hudson, R. L. Kurtz, and S. W. Robey, Phys. Rev. B **47**, 10832 (1993).
[12] N. B. Brookes, G. Thorton, and F. M. Quinn, Solid State Com-

mun. **64**, 383 (1987).
[13] K. Szot, J. Keppels, W. Speier, K. Besocke, M. Teske, and W. Eberhardt, Surf. Sci. **280**, 179 (1993).
[14] http://www.advancesoft.jp
[15] J. P. Perdew, J. A. Chevary, S. H. Vosko, K. A. Jackson, M. R. Pederson, and C. Fiolhais, Phys. Rev. B **46**, 6671 (1992).
[16] D. Vanderbilt, Phys. Rev. B **41**, 7892 (1990).
[17] H. J. Monkhorst and J. D. Pack, Phys. Rev. B **13**, 5188 (1976).
[18] M. Tutuianu, O. R. Inderwildi, W. G. Bessler, and J. Warnatz, J. Phys. Chem. B **110**, 17484 (2006).
[19] G. Pacchioni, Surf. Sci. **281**, 207 (1993).
[20] L. T. Hudson, R. L. Kurtz, S. W. Robey, D. Temple, and R. L. Stockbauer, Phys. Rev. B **47**, 1174 (1993).
[21] The sensitivity factors used were $S_{Sr}=1.843$, $S_{Ti}=2.001$, $S_O=0.711$, and $S_C=0.296$.
[22] R. P. Vasquez, M. C. Foote, and B. D. Hunt, J. Appl. Phys. **66**, 4866 (1989).
[23] T. Nishimura, A. Ikeda, H. Namba, T. Morishita, and Y. Kido, Surf. Sci. **421**, 273 (1999).
[24] V. Young and T. Otagawa, Appl. Surf. Sci. **20**, 228 (1985).
[25] V. E. Henrich and P. Cox, *The Surface Science of Metal Oxides* (Cambridge University Press, Cambridge, England, 2000), p. 250.
[26] D. Mueller, A. Shih, E. Roman, T. Madey, R. Kurtz, and R. Stockbauer, J. Vac. Sci. Technol. A **6**, 1067 (1988).
[27] C. T. Au, W. Hirsch, and W. Hirschwald, Surf. Sci. **199**, 507 (1988).
[28] T. Kawai, K. Kunimoki, T. Kondow, T. Onishi, and K. Tamaru, Z. Phys. Chem., Neue Folge **86**, 268 (1973).
[29] A. L. Cabrera, F. Vargas, and R. A. Zarate, J. Phys. Chem. Solids **55**, 1303 (1994).
[30] A. L. Cabrera, F. Vargas, R. A. Zarate, G. B. Cabrera, and J. Espinosa-Gangas, J. Phys. Chem. Solids **62**, 927 (2001).
[31] M. del Carmen Blanco Lopez, G. Fourlaris, B. Rand, and F. L. Riley, J. Am. Ceram. Soc. **82**, 1777 (1999).
[32] J. Padilla and D. Vanderbilt, Surf. Sci. **418**, 64 (1998).
[33] The rumpling parameter of the $i$th layer is defined as $S_i \equiv \delta Z(O)_i - \delta Z(M_i)$. The interlayer distance between cations of layers $i,j$ is defined as $\Delta d_{ij} \equiv \delta Z(M_i) - \delta Z(M_j)$.
[34] M.-Q. Cai, Y.-J. Zhang, G.-W. Yang, Z. Yin, M.-S. Zhang, W.-Y. Hu, and Y.-G. Wang, J. Chem. Phys. **124**, 174701 (2006).
[35] N. Bickel, G. Schmidt, K. Heinz, and K. Muller, Phys. Rev. Lett. **62**, 2009 (1989).
[36] R. Courths, J. Noffke, H. Wern, and R. Heise, Phys. Rev. B **42**, 9127 (1990).
[37] G. Pacchioni, J. M. Ricart, and F. Illas, J. Am. Chem. Soc. **116**, 10152 (1994).
[38] S. Azad, M. H. Englehard, and Li-Qiong Wang, J. Phys. Chem. B **109**, 10327 (2005).
[39] J. A. Rodriguez, S. Azad, L.-Q. Wang, J. Garcia, A. Etxeberria, and L. Gonzalez, J. Chem. Phys. **118**, 6562 (2003).
[40] The notations "=" and "⊥" refer to the directions shown in Figs. 6 and 7. The notation "=⊥"refers to the coexistence of both = and ⊥ components.
[41] X. J. Chen, G. Ouyang, C. C. Jia, L. L. Peng, C. K. Xu, S. X. Tian, and K. Z. Xu, J. Electron Spectrosc. Relat. Phenom. **107**, 273 (2000).
[42] J. W. Rabalais, J. M. McDonald, V. Scherr, and S. P. McGlynn, Chem. Rev. (Washington, D.C.) **71**, 73 (1971).
[43] H.-J. Freund and R. P. Messmer, Surf. Sci. **172**, 1 (1986).
[44] J. A. Tossell, J. Phys. Chem. Solids **37**, 1043 (1976).
[45] M. Wegmann, L. Watson, and A. Hendry, J. Am. Ceram. Soc. **87**, 371 (2004).